# SUPPORTING INFORMATION

# An isotropic zero thermal expansion alloy with super-high toughness

Chengyi Yu[1], Kun Lin[1], Qinghua Zhang[2], Huihui Zhu[1], Ke An[3], Yan Chen[3], Dunji Yu[3], Tianyi Li[4], Xiaoqian Fu[5], Qian Yu,[5] Li You[1], Xiaojun Kuang[6], Yili Cao[1], Qiang Li[1], Jinxia Deng[1] and Xianran Xing[1,*]


[1] Beijing Advanced Innovation Center for Materials Genome Engineering, and Institute of Solid State Chemistry, University of Science and Technology Beijing, Beijing 100083, China.

[2] Institution of Physics, Chinese Academic of Science, No.8, 3rd South Street, Zhongguancun, Haidian District, Beijing, 100190 P. R. China.

[3] Neutron Scattering Division, Oak Ridge National Laboratory, Oak Ridge, TN, USA.

[4] X-Ray Science Division, Argonne National Laboratory, Argonne, IL 60439, USA

[5] Center of Electron Microscopy and State Key Laboratory of Silicon Materials, Department of Materials Science and Engineering, Zhejiang University, Hangzhou, China.

[6] Guangxi Key Laboratory of Electrochemical and Magnetochemical Functional Materials, College of Chemistry and Bioengineering, Guilin University of Technology, Guilin 541004, P. R. China.

*Corresponding author. Email: *xing@ustb.edu.cn*

# Contents

**Supplementary Tables**

**Supplementary Table 1 | The chemical composition of elements of the LaFe$_{43.5+x}$Si$_{2.6+0.06x}$ ($x$ = 0, 4, 8, 12, 16) series alloys which were attained by EPMA.**

| Compositions | α Phase, elements atom% | | | L Phase, elements atom% | | | Partition coefficient | |
|---|---|---|---|---|---|---|---|---|
| | Si | Fe | La | Si | Fe | La | Si$_L$/Si$_α$ | Fe$_L$/Fe$_α$ |
| | 3.162 | 96.733 | 0.104 | 11.731 | 82.457 | 5.812 | 3.709 | 0.852 [①] |
| LaFe$_{43.5}$Si$_{2.6}$ | 3.159 | 96.649 | 0.191 | 11.834 | 82.398 | 5.769 | 3.746 | 0.852 [②] |
| | 3.622 | 96.285 | 0.093 | 12.022 | 82.343 | 5.6345 | 3.319 | 0.855 [③] |
| | 3.158 | 96.721 | 0.121 | 11.953 | 82.206 | 5.505 | 3.785 | 0.850 [①] |
| LaFe$_{47.5}$Si$_{2.84}$ | 3.121 | 96.719 | 0.159 | 11.980 | 82.206 | 5.484 | 3.839 | 0.850 [②] |
| | 3.274 | 96.548 | 0.176 | 11.844 | 82.354 | 5.470 | 3.617 | 0.853 [③] |
| | 3.719 | 96.279 | 0.055 | 12.099 | 87.170 | 6.035 | 3.253 | 0.905 [①] |
| LaFe$_{51.5}$Si$_{3.08}$ | 3.737 | 96.260 | 0.072 | 12.264 | 86.989 | 6.091 | 3.282 | 0.904 [②] |
| | 3.766 | 96.231 | 0.090 | 11.972 | 87.304 | 6.049 | 3.180 | 0.907 [③] |
| | 4.204 | 95.132 | 0.663 | 12.940 | 81.403 | 5.656 | 3.078 | 0.856 [①] |
| LaFe$_{55.5}$Si$_{3.32}$ | 4.172 | 95.714 | 0.113 | 13.159 | 81.181 | 5.658 | 3.154 | 0.848 [②] |
| | 4.311 | 95.570 | 0.119 | 12.512 | 81.769 | 5.719 | 2.902 | 0.856 [③] |
| | 4.104 | 95.819 | 0.077 | 12.743 | 81.562 | 5.695 | 3.105 | 0.851 [①] |
| LaFe$_{59.5}$Si$_{3.56}$ | 4.043 | 95.855 | 0.101 | 12.332 | 82.013 | 5.654 | 3.050 | 0.856 [②] |
| | 3.927 | 96.023 | 0.049 | 12.212 | 82.213 | 5.575 | 3.109 | 0.856 [③] |

Average ratio Si$_L$/Si$_α$: 3.342; Fe$_L$/Fe$_α$: 0.863

Note：①、②、③ represent that three separate area collections were selected for each sample.

**Supplementary Table 2 | The chemical composition of elements of the $LaFe_{0.939x}Co_{0.061x}Si_{0.0583x}$ ($x$ = 37.5, 47.5, 57. and 67.5, labeled as S-1, S-2, S-3, and S-4, respectively) series alloys which were attained by EPMA.**

| Compositions | α Phase, elements atom% | | | | L Phase, elements atom% | | | | Partition coefficient | | |
|---|---|---|---|---|---|---|---|---|---|---|---|
| | Co | Si | Fe | La | Co | Si | Fe | La | $Si_L/Si_\alpha$ | $Fe_L/Fe_\alpha$ | $Co_L/Co_\alpha$ |
| | 5.281 | 2.383 | 92.256 | 0.080 | 6.699 | 10.116 | 77.493 | 5.692 | 4.245 | 0.840 | 1.268 [①] |
| S-1 | 5.277 | 2.476 | 92.157 | 0.090 | 6.639 | 10.089 | 77.904 | 5.368 | 4.075 | 0.845 | 1.258 [②] |
| | 5.348 | 2.496 | 92.024 | 0.133 | 6.828 | 10.416 | 77.004 | 5.752 | 4.173 | 0.837 | 1.277 [③] |
| | 5.431 | 3.064 | 91.367 | 0.137 | 6.854 | 11.547 | 76.009 | 5.591 | 3.769 | 0.832 | 1.262 [①] |
| S-2 | 5.452 | 3.140 | 91.256 | 0.152 | 6.981 | 11.517 | 75.853 | 5.65 | 3.668 | 0.831 | 1.280 [②] |
| | 5.499 | 3.053 | 91.288 | 0.160 | 6.833 | 10.933 | 76.932 | 5.302 | 3.581 | 0.843 | 1.243 [③] |
| | 5.452 | 3.390 | 91.064 | 0.094 | 6.956 | 11.624 | 75.764 | 5.656 | 3.429 | 0.832 | 1.276 [①] |
| S-3 | 5.505 | 3.307 | 91.100 | 0.088 | 6.682 | 11.019 | 78.044 | 4.255 | 3.332 | 0.857 | 1.214 [②] |
| | 5.519 | 3.423 | 90.965 | 0.093 | 6.915 | 11.862 | 75.989 | 5.234 | 3.465 | 0.835 | 1.253 [③] |
| | 5.616 | 3.535 | 90.752 | 0.097 | 7.196 | 12.189 | 74.723 | 5.891 | 3.448 | 0.823 | 1.281 [①] |
| S-4 | 5.626 | 3.551 | 90.759 | 0.064 | 7.047 | 12.428 | 74.994 | 5.531 | 3.500 | 0.826 | 1.253 [②] |
| | 5.621 | 3.515 | 90.800 | 0.064 | 7.131 | 12.020 | 75.286 | 5.562 | 3.420 | 0.829 | 1.269 [③] |

Average ratio $Si_L/Si_\alpha$: 3.675; $Fe_L/Fe_\alpha$: 0.836; $Co_L/Co_\alpha$: 1.261

Note：①、②、③ represent that three separate area collections were selected for each sample.

**Supplementary Table 3 | The summary of ultimate strength ($\delta_{US}$, MPa) and strain ($\varepsilon_f$, %) in typical ZTE materials.**

| Typical ZTE materials | Strain ($\varepsilon_f$, %) | Ultimate strength ($\delta_{US}$, MPa) | References |
|---|---|---|---|
| $TbCo_{1.9}Fe_{0.1}$ | 1.5 | 260 | [1] |
| $Ho_2Fe_{16}Cr$ | 2.0 | 50 | [2] |
| MnCoGe | 1.0 | 70.4 | [3] |
| $LaFe_{11}Si_2H_x$ | 1.0 | 60 | [4] |
| $Mn_3Cu_{0.5}Ge_{0.5}N$ | 1.0 | 161 | [5] |
| $Hf_{0.87}Ta_{0.13}Fe_2$ | 2.7 | 380 | [6] |
| $Mn_3Ge_{0.9}Sn_{0.1}$ | 5.0 | 450 | [7] |
| $Mn_3Ge$ | 5.6 | 204 | [7] |
| $Ho_{0.07}Fe_{0.93}$ | 5.68 | 1275.8 | [8] |
| $Ho_{0.05}Fe_{0.95}$ | 8.08 | 796.8 | [8] |
| $Ho_{0.04}Fe_{0.96}$ | 15.6 | 878 | [8] |
| GDFC | 1.2 | 154 | [9] |
| $LaFe_{14.2}Co_{1.2}Si_{1.6}$ | 3.2 | 861.1 | [10] |
| $LaFe_{16.2}Co_{1.2}Si_{1.6}$ | 3.6 | 883.6 | [10] |
| $LaFe_{18.2}Co_{1.2}Si_{1.6}$ | 3.78 | 968.8 | [10] |
| $LaFe_{20.2}Co_{1.2}Si_{1.6}$ | 3.87 | 1001.6 | [10] |
| $LaFe_{10.1}Cu_{0.5}Si_{2.4}$ | 2.8 | 1325 | [11] |
| $LaFe_{10.2}Cu_{0.4}Si_{2.4}$ | 2.6 | 1240 | [11] |
| $La(Fe, Co, Si)_{13}/Cu_{54.6}$ | 12.6 | 441.1 | [12] |
| $La(Fe, Co, Si)_{13}/Cu_{39.7}$ | 6.4 | 360.6 | [12] |
| $La(Fe, Co, Si)_{13}/Cu_{25.6}$ | 1.9 | 218.5 | [12] |
| $La(Fe, Si)_{13}/Resin_3$ | 4.2 | 116.2 | [13] |
| $La(Fe, Si)_{13}/Resin_{20}$ | 4.1 | 180.9 | [13] |
| $La(Fe, Si)_{13}/Resin_{80}$ | 5.3 | 203.8 | [13] |
| $Ho_2Fe_{16}Co$ | 2 | 49 | [14] |
| Er-Fe-V-Mo | 2.31 | 1631.4 | [15] |
| $La(Fe, Co, Si)_{13}$ | 1.6 | 256.4 | [16] |
| S-3 | 30.9 | 1110.1 | This work |
| Invar | 30 | 680.0 | $\varepsilon = 30\%$ |

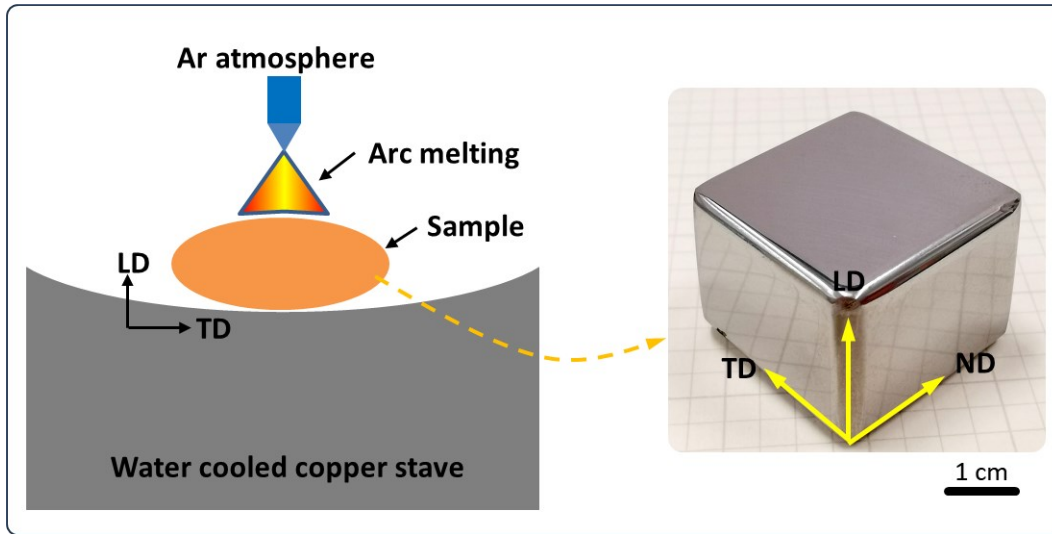# Supplementary Figures
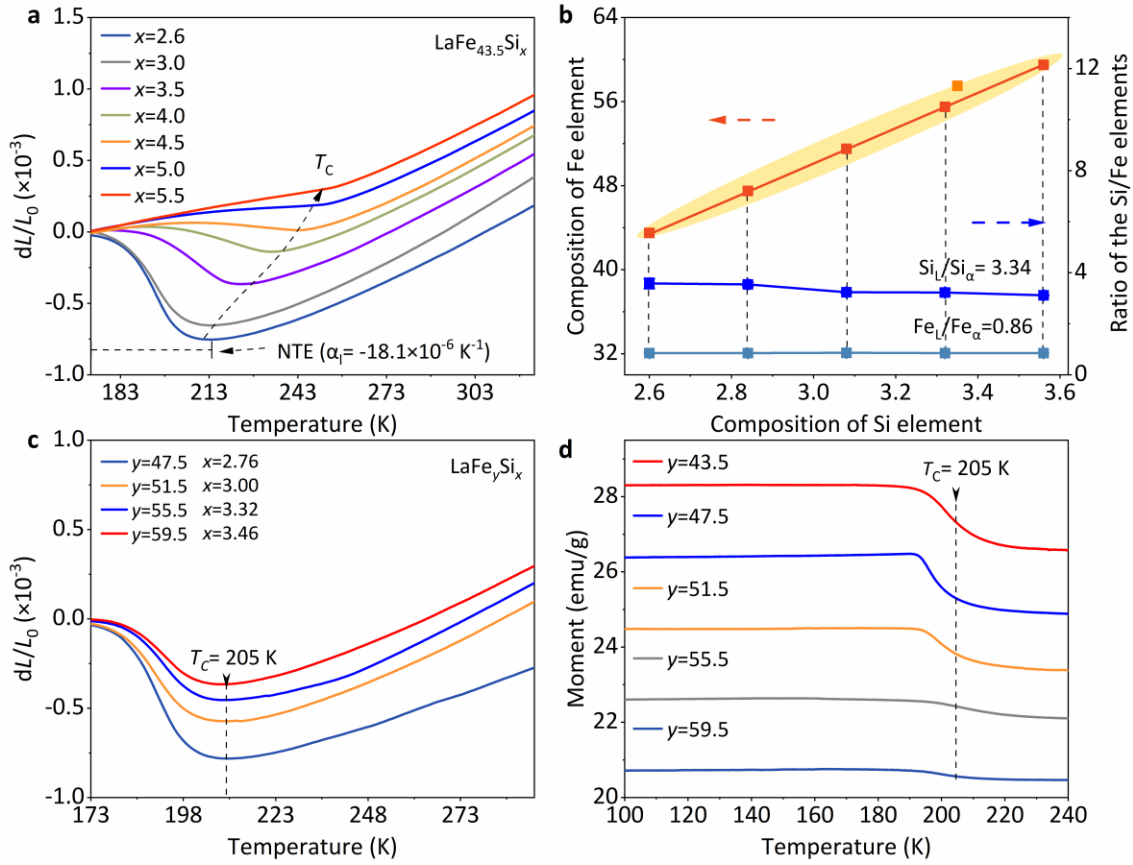


**Supplementary Fig. 1 | The calculation of $Si_L/Si_\alpha$ and $Fe_L/Fe_\alpha$ partition coefficient in La-Fe-Si ternary system. a**, The dilatometer thermal expansion of series $LaFe_{43.5}Si_x$ ($x$ = 2.6, 3.0, 3.5, 4.0, 4.5, 5.0, 5.5) alloys. **b**, The ratio of $Si_L/Si_\alpha$ and $Fe_L/Fe_\alpha$ in response to different compositions. **c**, The dilatometer thermal expansion of series $LaFe_{43.5+x}Si_{2.6+0.06x}$ ($x$ = 0, 4, 8, 12, 16) alloys. **d**, The corresponding magnetic measurements of the series alloys.

6
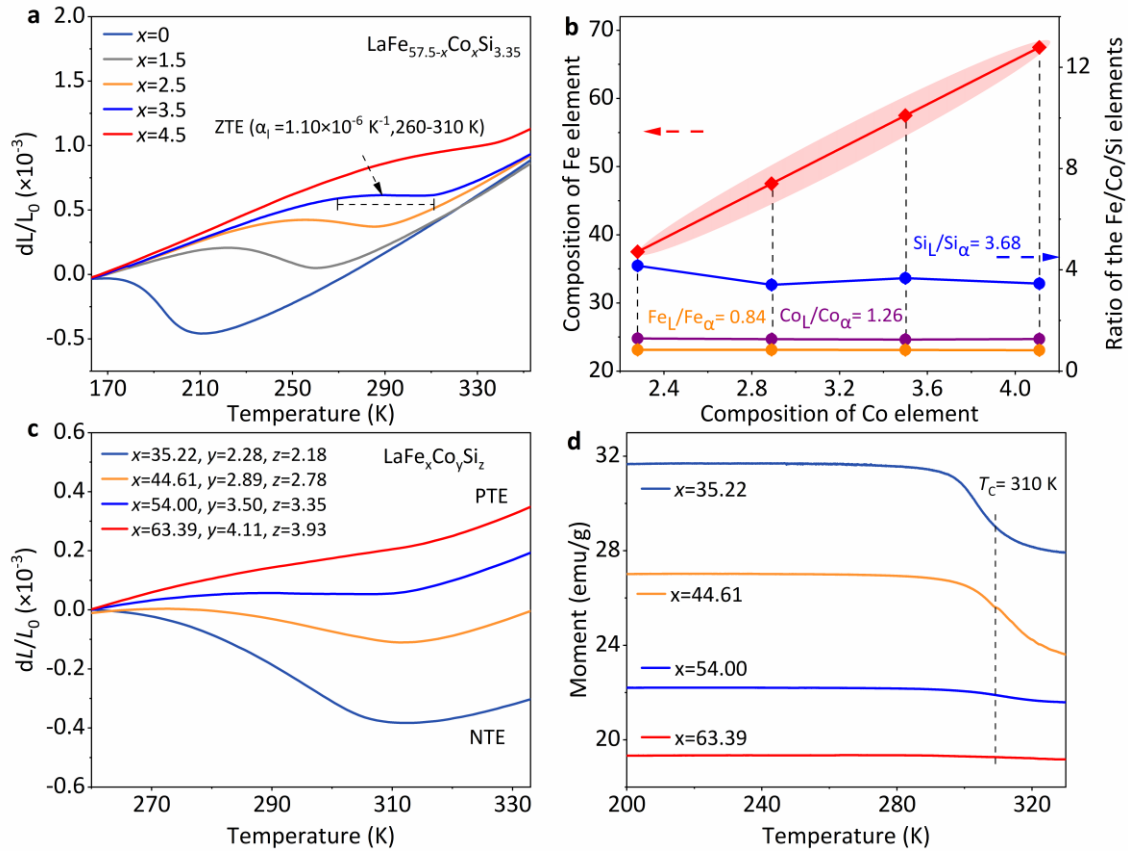
**Supplementary Fig. 2 | The calculation of $Si_L/Si_\alpha$, $Fe_L/Fe_\alpha$ and $Co_L/Co_\alpha$ partition coefficient.**
**a**, The dilatometer thermal expansion of series $LaFe_{57.5-x}Co_xSi_{3.35}$ ($x$ = 0, 1.5, 2.5, 3.5, 4.5) alloys.
**b**, The ratio of $Si_L/Si_\alpha$, $Fe_L/Fe_\alpha$, and $Co_L/Co_\alpha$ in response to different compositions. **c**, The dilatometer thermal expansion of series $LaFe_{57.5-x}Co_xSi_{3.35}$ ($x$ = 0, 1.5, 2.5, 3.5, 4.5) alloys. **d**, The corresponding magnetic measurements of the series alloys.

**Supplementary Fig. 3 | Schematic diagram of the relationship between ingot and coordinate system.** The temperature gradient along the LD direction is the reason for the preferential growth of the sample.
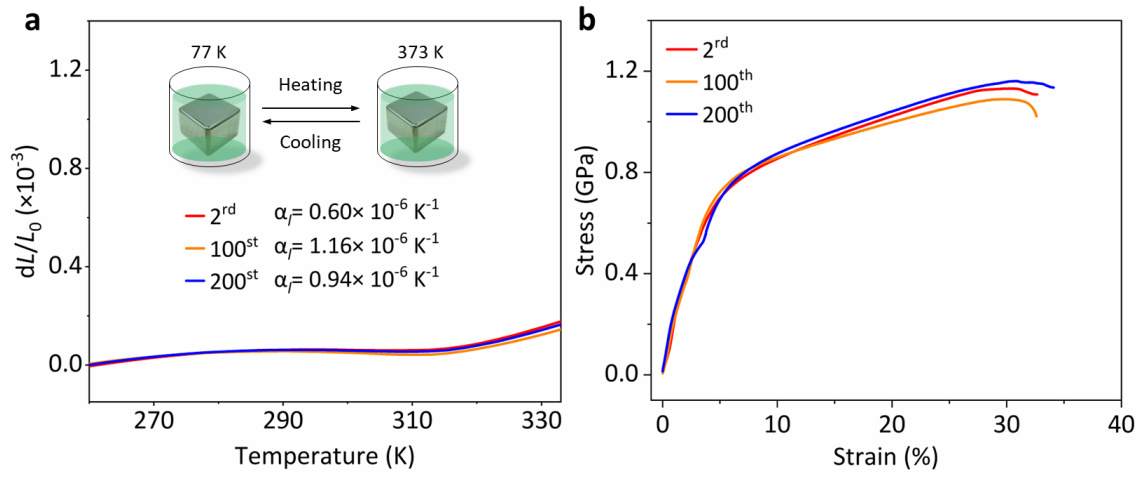
**Supplementary Fig. 4 | The cyclic thermal shock experiment undergoes a thermal shock from 77 K to 373 K. a**, The dilatometer thermal expansions of S-3 alloy in the 1st, 100th, and 200th cycles. **b**, The compressive stress-strain curves of the S-3 alloy after the 1st, 100th, and 200th cycles.
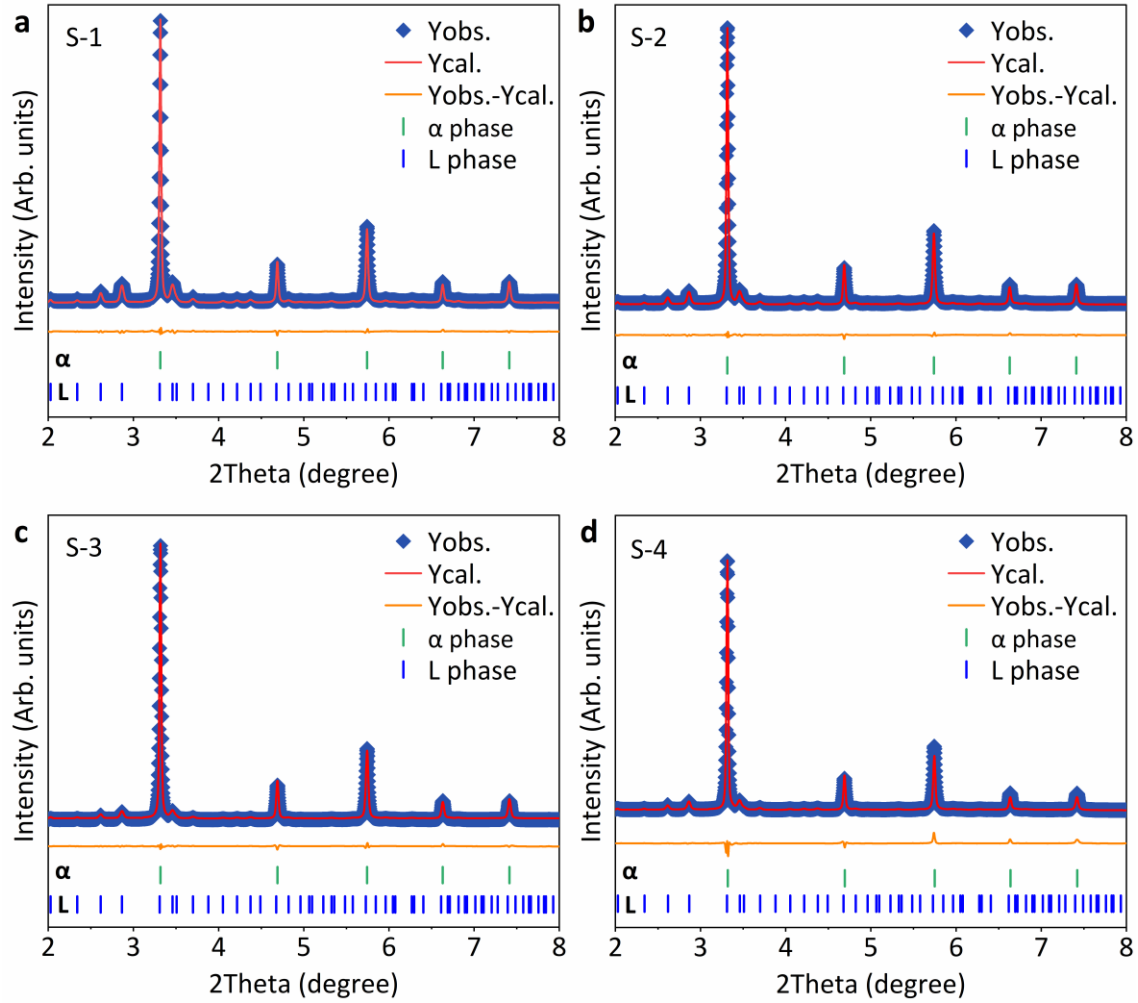
**Supplementary Fig. 5 | a-d,** The Rietveld refinement of synchrotron X-ray diffraction profile of the as-cast samples in composition $LaFe_{0.939x}Co_{0.061x}Si_{0.0583x}$ ($x = 37.5$, $47.5$, $57.5$, and $67.5$, labeled as S-1, S-2, S-3, and S-4, respectively).
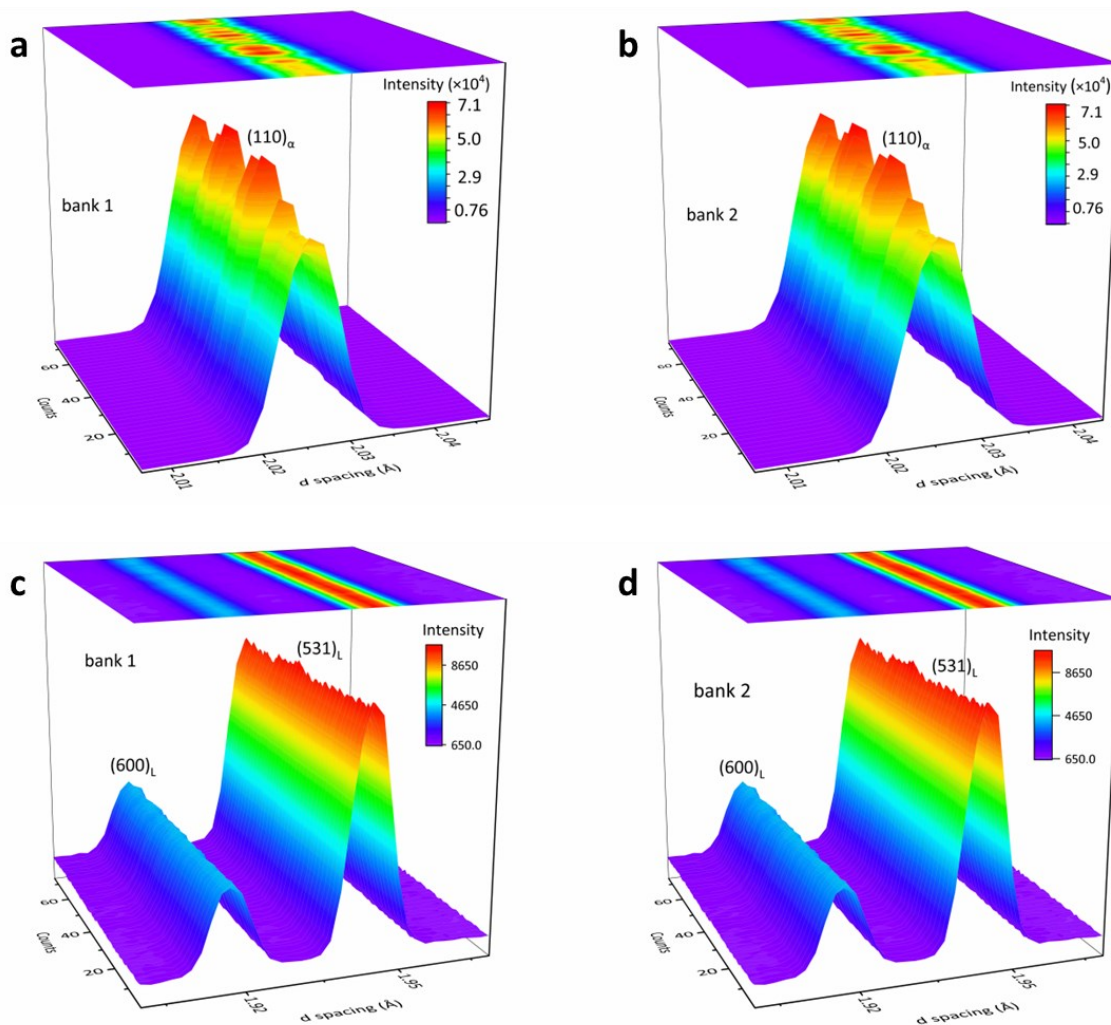
**Supplementary Fig. 6 | The typical diffraction (*hkl*) reflections of the dual-phase alloy. a-b**, The $(110)_\alpha$ reflection was collected by bank 1 and bank 2 detectors, respectively. **c-d**, The $(600)_L$ and $(531)_L$ reflections were collected by bank 1 and bank 2 detectors, respectively. The 75 counts are used to collect the three-dimensional crystallographic information (11.25 degrees/step for 45-degree vertical rotation; 24 degrees/step for 336-degree horizontal rotation). At each step, the two detectors will be collected, respectively.
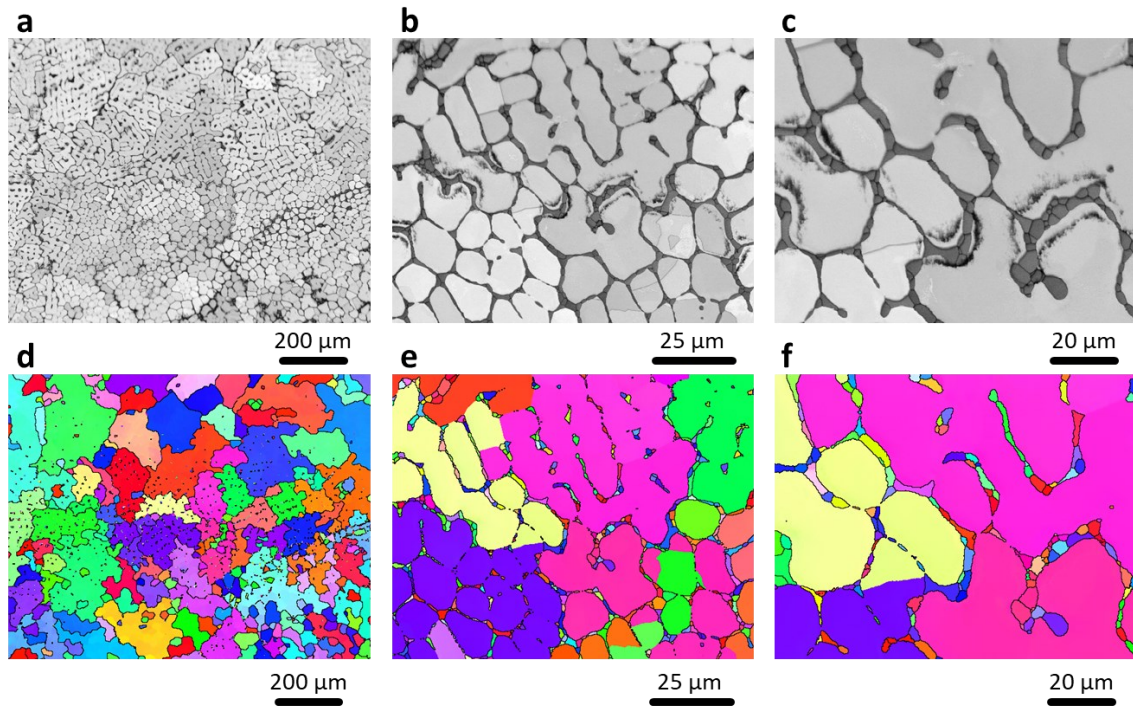
**Supplementary Fig. 7 | The microstructure and inverse pole figure (IPFZ) of S-3 alloy. a-c**, The EBSD band contrast figure at different magnifications. **d-f**, The EBSD inverse pole figure (IPFZ) at different magnifications.
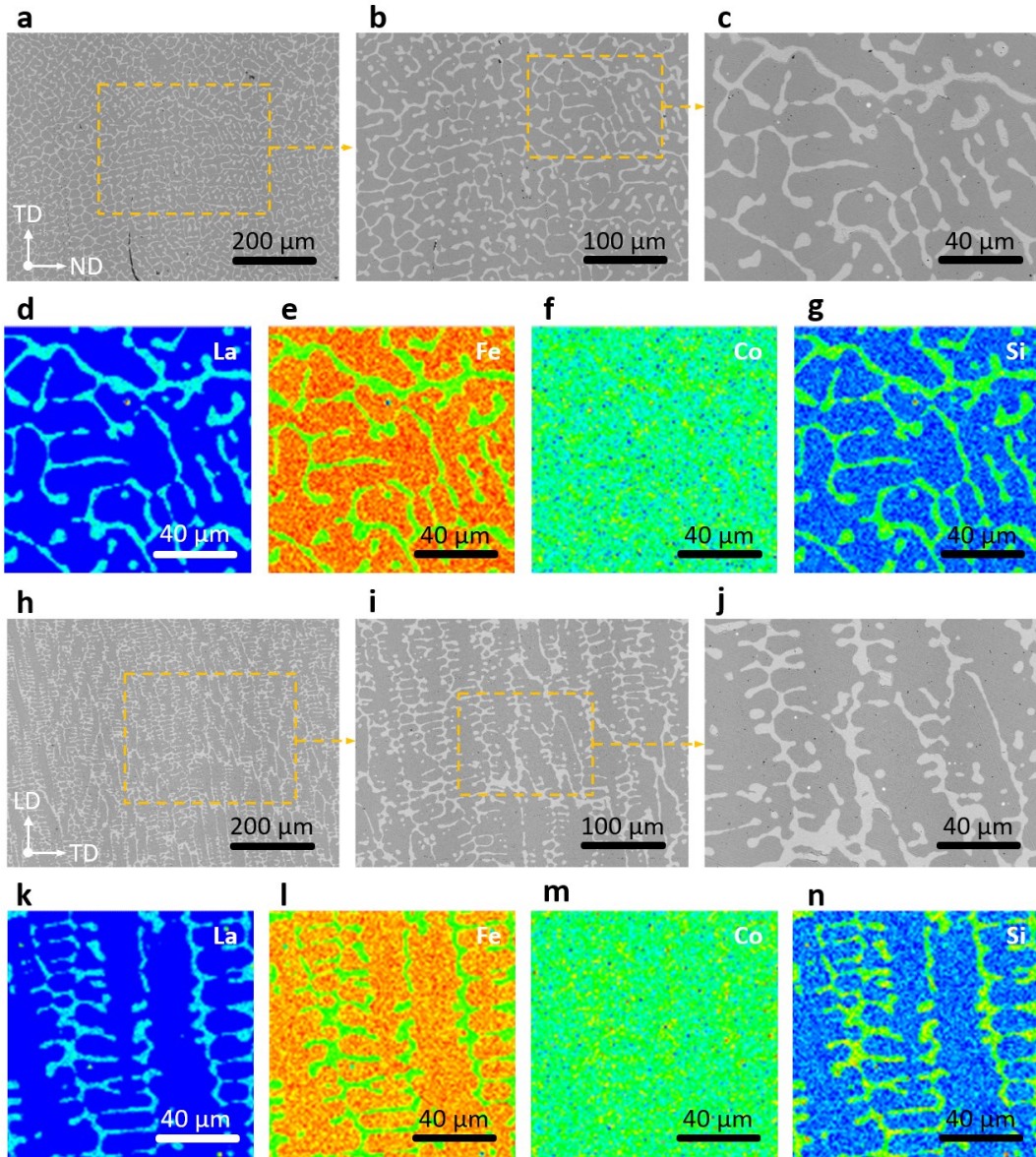
**Supplementary Fig. 8 | The electro-probe micro-analyzer (EPMA) mappings of the S-3. a-c**, The microstructure of S-3 in TD-ND plane at different magnifications. **d-g**, the elements mapping of La, Fe, Co, and Si, respectively. **h-j**, The microstructure of S-3 in LD-TD plane at different magnifications. **k-n**, the elements mapping of La, Fe, Co, and Si, respectively. We observed that there are certain differences in the morphology of the alloy (S-3) between the in-plane (TD-ND) and out-of-plane (LD-TD), the in-plane appearance is a continuous network and the out-of-plane shape is dendritic, which may be related to the growth direction of the as-cast alloy. As a result, the dilatometer thermal expansion behaves a negligible differences.
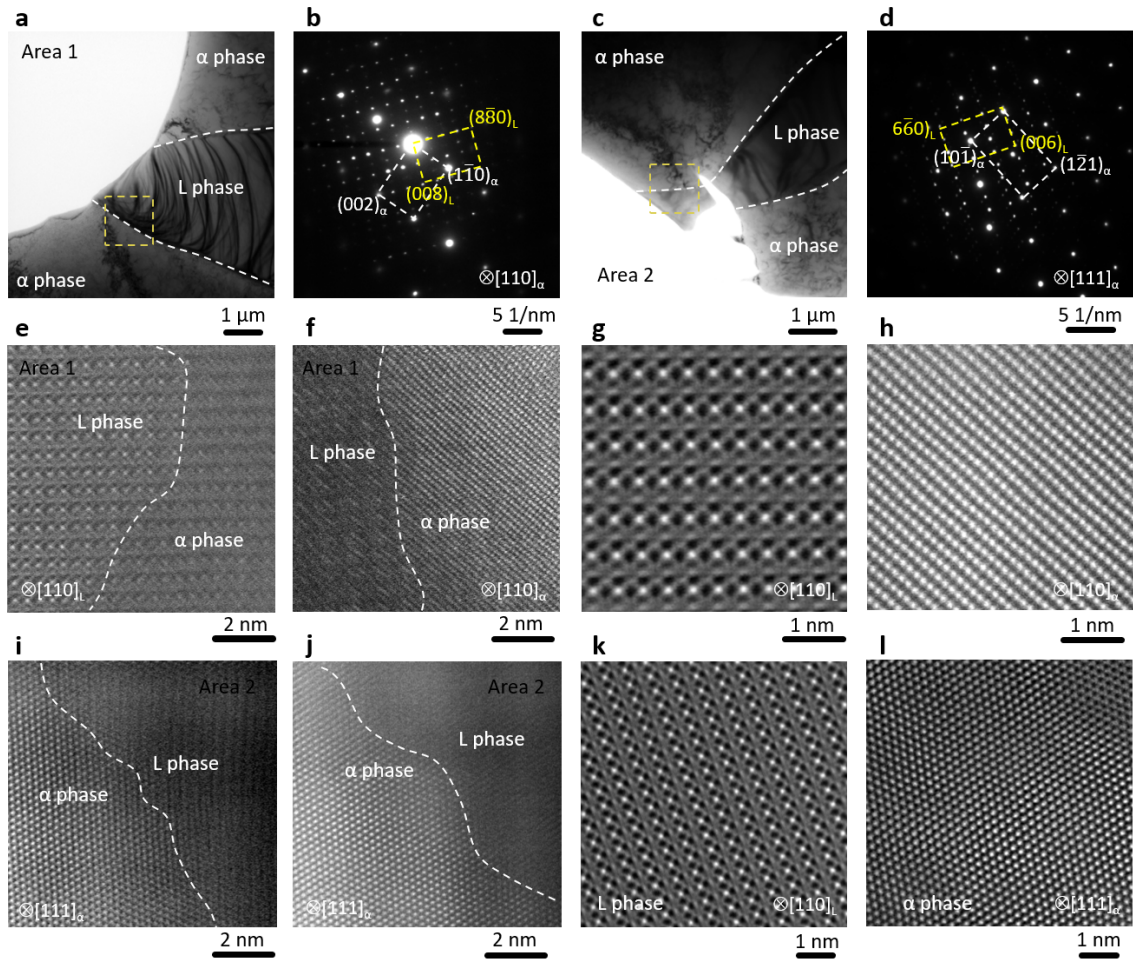
**Supplementary Fig. 9 | The interface structure of the S-3alloy. a-d**, The phase interfaces of the alloy and corresponding selected area electron diffraction (SAED). **e-l**, The HAADF-STEM images at the phase interface.

14
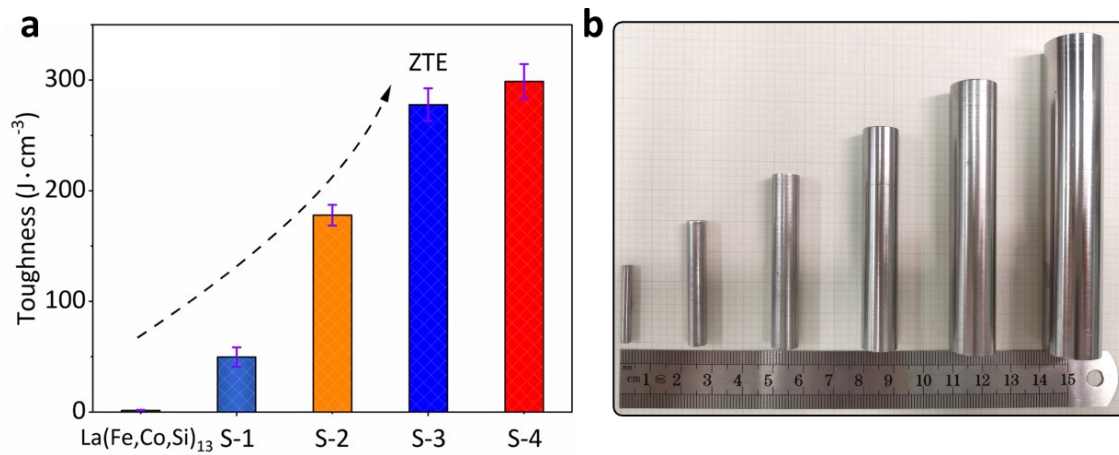
**Supplementary Fig. 10 | Mechanical performance and small parts. a**, Toughness comparison of S-1, S-2, S-3, and S-4 series alloys and targeted synthesis of the L phase. **b**, The super-high toughness S-3 alloy is facile and precisely to be machined. The rods/tubes are melted under induction melting conditions and cast into $\Phi$ 25 mm diameter rods, annealed under vacuum (1373 K + 24 hours), then machined to a suitable size and surface polished.
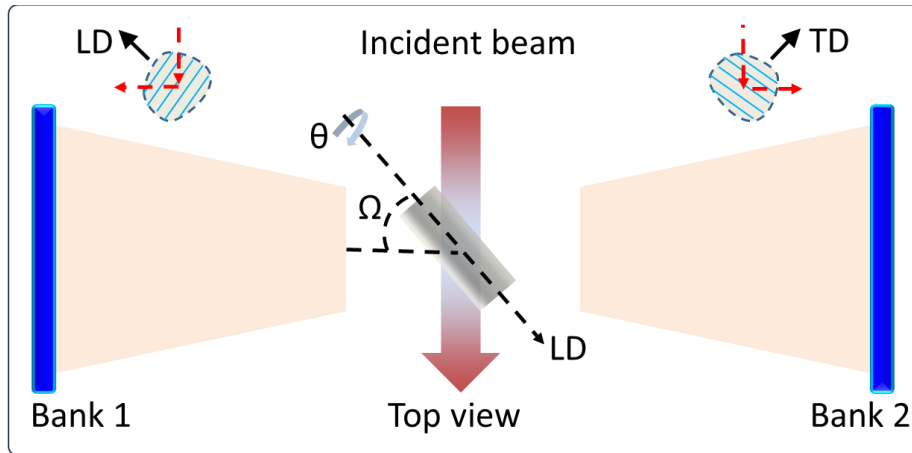
**Supplementary Fig. 11 | Schematic diagram of the in-situ neutron diffraction experimental set-up from the top view.** The sample is horizontal and positioned at 45° from the incident beam such that Bank 1 probes the strain component along the LD, while Bank 2 simultaneously probes the strain component in the TD, as shown in two insets.
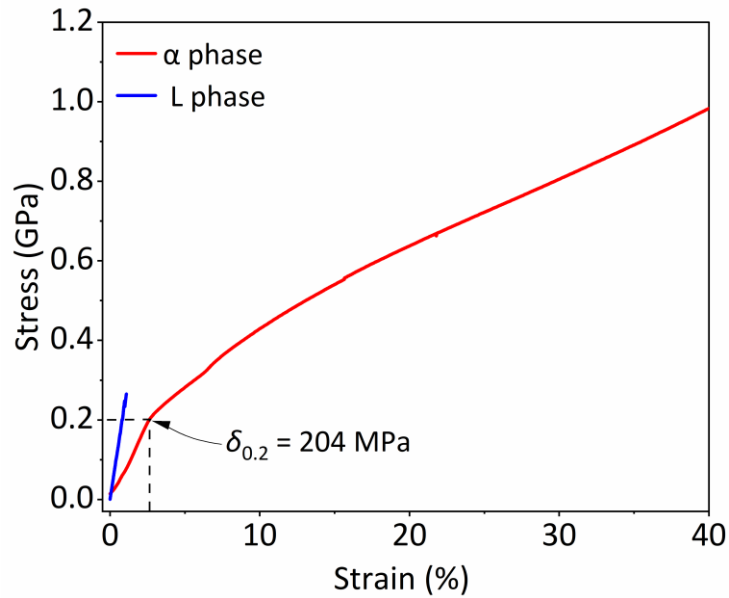
**Supplementary Fig. 12 | The compressive stress-strain curves of the pure L phase ($LaFe_{10.30}Co_{0.83}Si_{1.87}$) and α phase ($Fe_{92.42}Co_{4.34}Si_{3.07}$).** The L phase shows brittle but negative thermal expansion, and the α phase behaves as plastic and has positive negative thermal expansion.
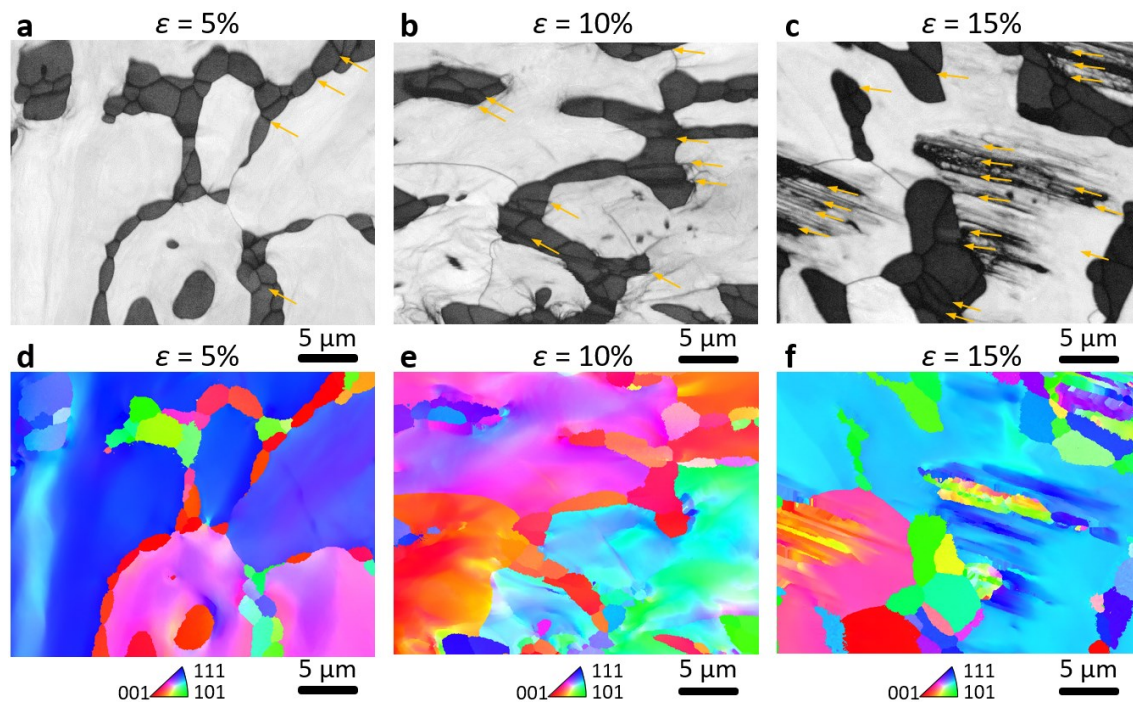
**Supplementary Fig. 13 | Microstructure evolution of the dual-phase alloy (ZTE composition).**
**a-c,** Ex-situ EBSD phase contrast image under 5%, 10%, 15% strain ($\varepsilon$) conditions. Orange arrows represent shear cracks. **d-f,** Ex situ EBSD IPF inverse pole image under 5%, 10%, 15% strain ($\varepsilon$) conditions.
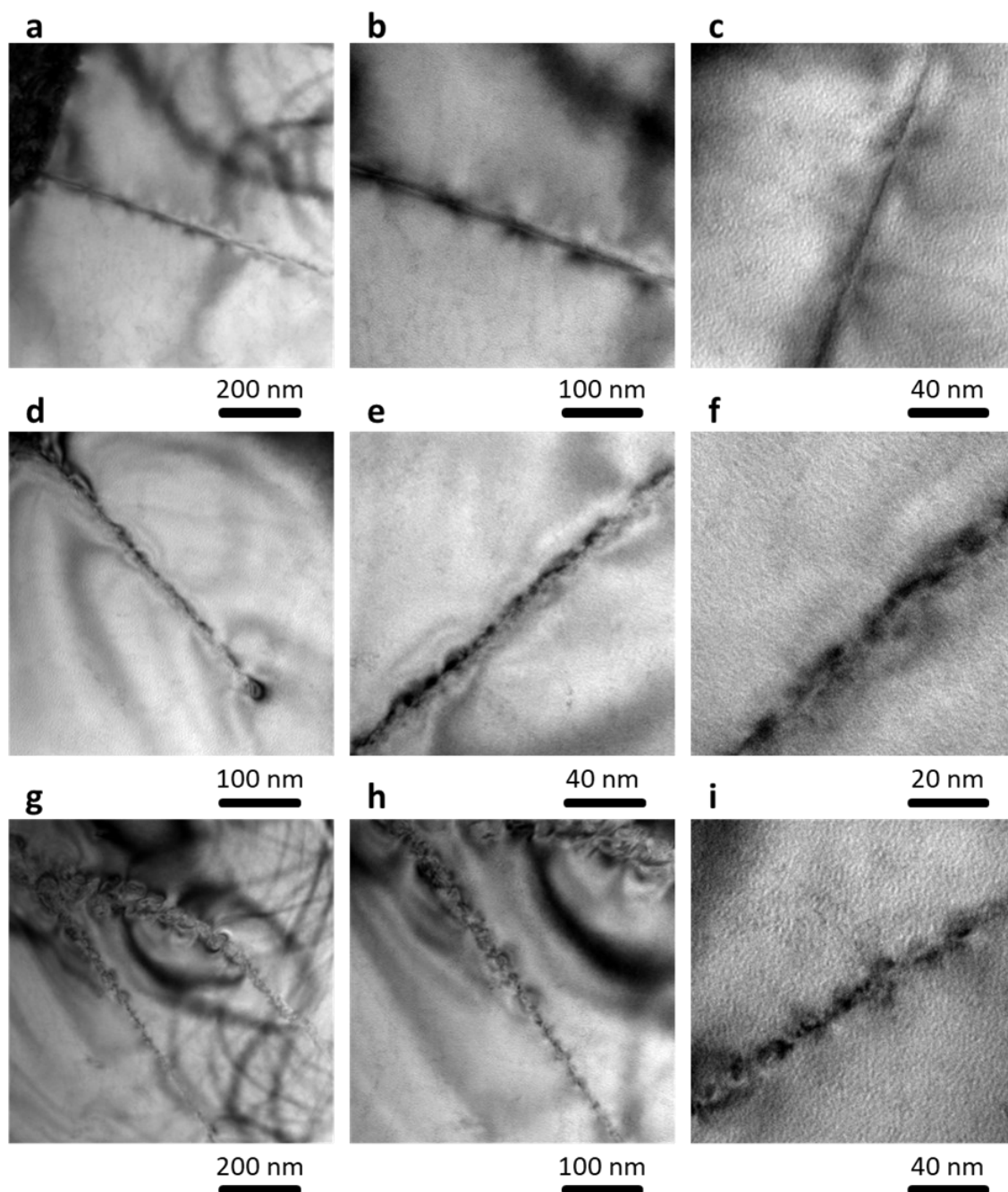
**Supplementary Fig. 14 | Microstructure evolution of the dual-phase alloy (ZTE composition).**
**a-c,** Different stacking faults observed in the L phase at 5% strain ($\varepsilon$). This indicates that stacking faults are the main deformation mechanism in the initial stage of L-phase plastic deformation. **d-f,** Dual-phase interface structures at 15% strain ($\varepsilon$). The microcracks in the L phase are hindered from propagating to the interface.
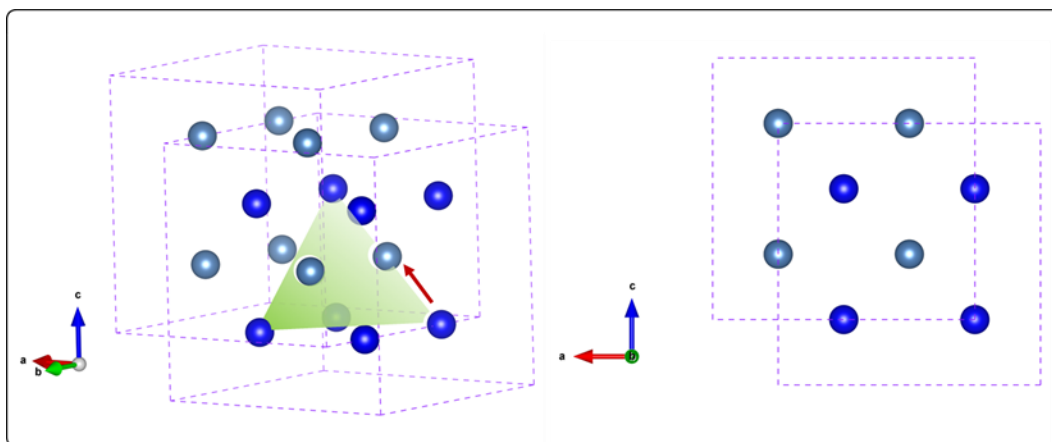
**Supplementary Fig. 15 | The evolution of stacking fault illustrated by the crystal structure.** To make the model clearer, we only keep La atoms here.
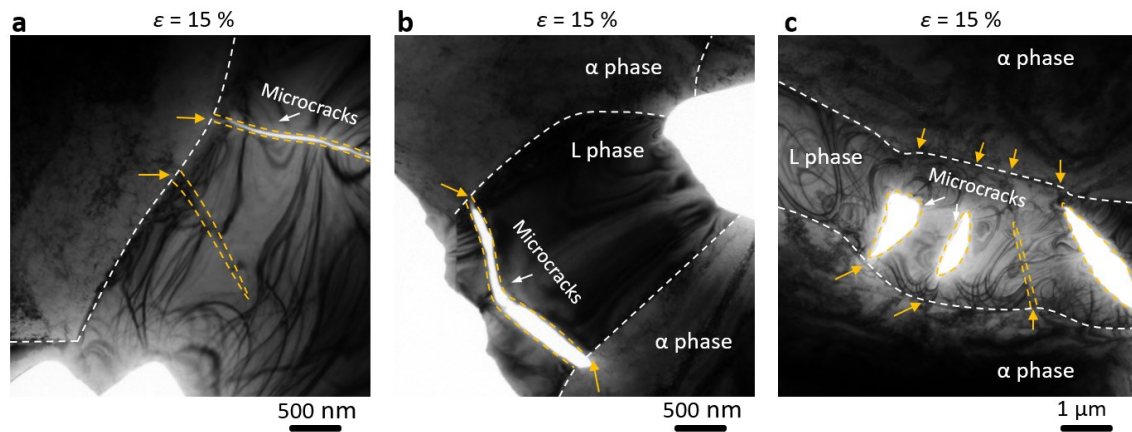
**Supplementary Fig. 16 | a-c, Dual-phase interface structures at 15% strain ($\varepsilon$).** The microcracks in the L phase are hindered from propagating to the interface. Noted: The cracks were affected by the thinning process. Noted: The structure of the cracks is affected to varying degrees by the thinning process.
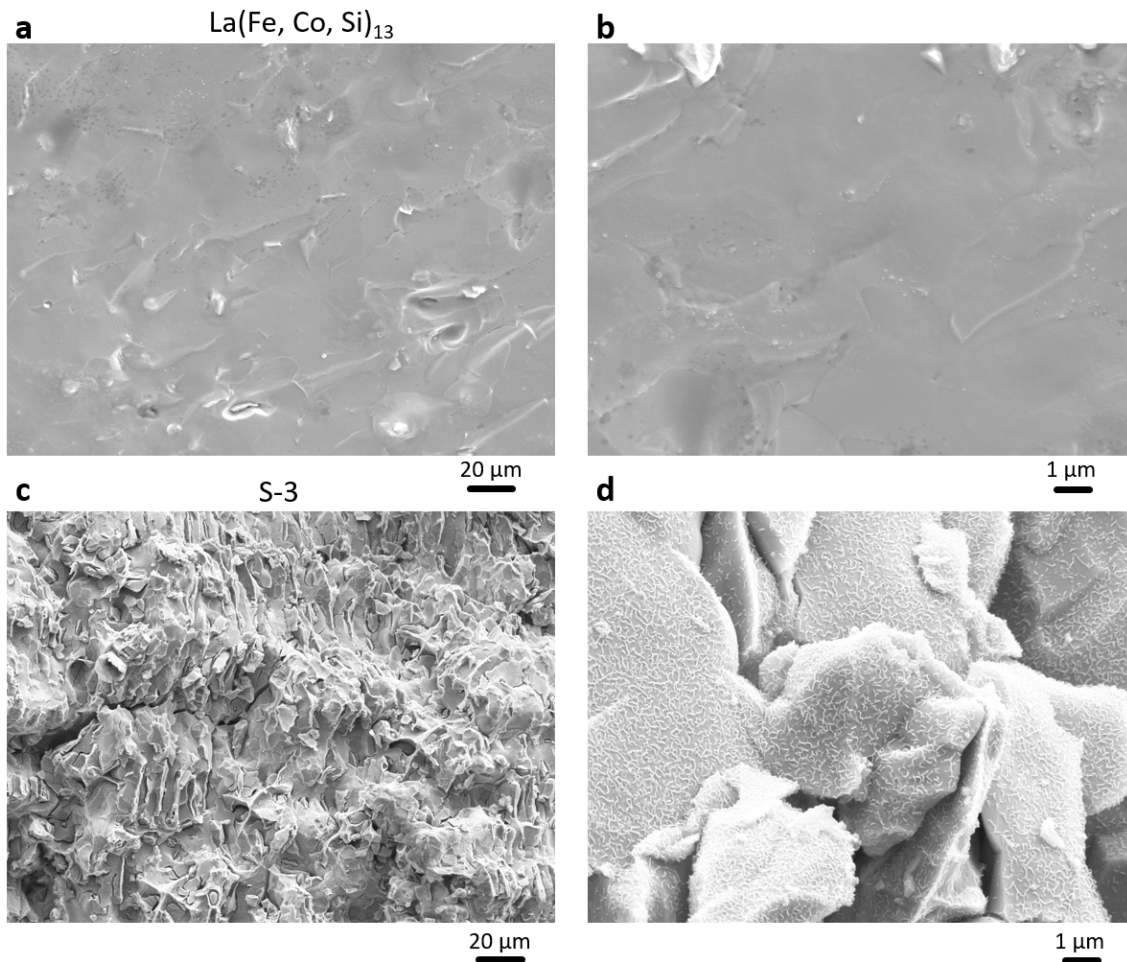
**Supplementary Fig. 17 | a-d,** Fracture morphology of the S-3 and pure La(Fe, Co, Si)$_{13}$ compound, dense and cross stripes demonstrated the large plastic deformation before failure.
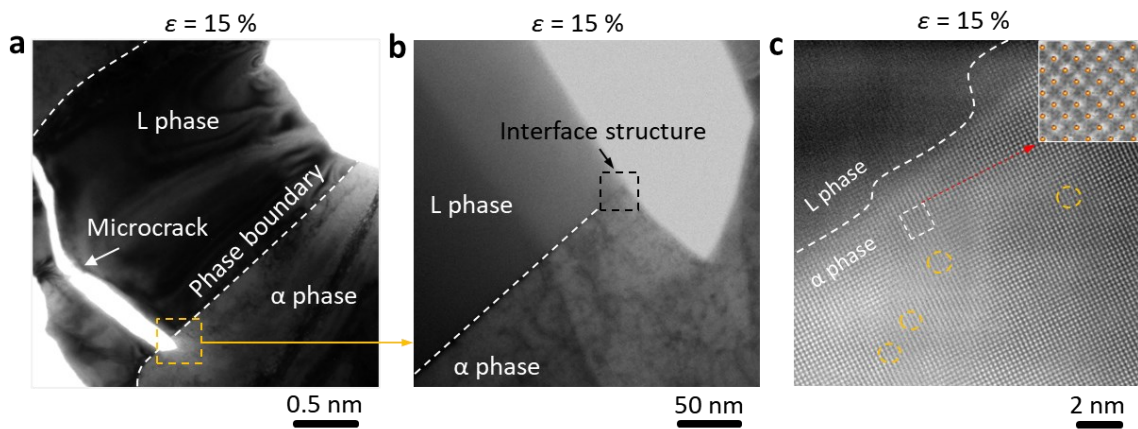
**Supplementary Fig. 18 | A typical interface of the dual-phase alloy (ZTE composition) at 15 % strain ($\varepsilon$). a-c**, The interface structure of the dual-phase alloy is determined by TEM at different scales.

## Supplementary References

1. Song, Y., *et al.* Zero thermal expansion in magnetic and metallic Tb(Co,Fe)$_2$ intermetallic compounds. *J. Am. Chem. Soc.* **140**, 602-605 (2018).
2. Dan, S., *et al.* Zero thermal expansion with high Curie temperature in Ho$_2$Fe$_{16}$Cr alloy. *RSC Adv.* **6**, 94809-94814 (2016).
3. Zhao, Y., *et al.* Giant negative thermal expansion in bonded MnCoGe-based compounds with Ni$_2$In-type hexagonal structure. *J. Am. Chem. Soc.* **137**, 1746-1749 (2015).
4. Li, S., *et al.* Zero thermal expansion achieved by an electrolytic hydriding method in La(Fe,Si)$_{13}$ Compounds. *Adv. Funct. Mater.* **27**, 1604195 (2017).
5. Song, X., *et al.* Adjustable zero thermal expansion in antiperovskite manganese nitride. *Adv. Mater.* **23**, 4690-4694 (2011).
6. Li, L., *et al.* Good comprehensive performance of Laves phase Hf$_{1-x}$Ta$_x$Fe$_2$ as negative thermal expansion materials. *Acta Mater.* **161**, 258-265 (2018).
7. Song, Y., *et al.* Opposite thermal expansion in isostructural noncollinear antiferromagnetic compounds of Mn$_3$A (A = Ge and Sn). *Chem. Mater.* **30**, 6236-6241 (2018).
8. Yu, C., *et al.* Plastic and low-cost axial zero thermal expansion alloy by a natural dual-phase composite. *Nat. Commun.* **12**, 4701 (2021).
9. Hu, J., *et al.* Adjustable magnetic phase transition inducing unusual zero thermal expansion in cubic RCo$_2$-based intermetallic compounds (R = Rare Earth). *Inorg. Chem.* **58**, 5401-5405 (2019).
10. Wang, J., *et al.* Balancing negative and positive thermal expansion effect in dual-phase La(Fe,Si)$_{13}$/α-Fe in-situ composite with improved compressive strength. *J. Alloy Compd.* **769**, 233-238 (2018).
11. Liu, J., *et al.* Realization of zero thermal expansion in La(Fe,Si)$_{13}$ -based system with high mechanical stability. *Mater. Design.* **148**, 71-77 (2018).
12. Pang, X., *et al.* Design of zero thermal expansion and high thermal conductivity in machinable *x*LFCS/Cu metal matrix composites. *Compos. Part B-Eng.* **238**, 109883 (2022).
13. Zhou, H., *et al.* Tunable negative thermal expansion in La(Fe, Si)$_{13}$/resin composites with high mechanical property and long-term cycle stability. *Microst.* **2**, 1-15 (2022).
14. Cao, Y., *et al.* Ultrawide temperature range super-Invar behavior of R$_2$(Fe,Co)$_{17}$ materials (R = Rare Earth). *Phys. Rev. Lett.* **127**, 055501 (2021).
15. Lin, K., *et al.* High performance and low thermal expansion in Er-Fe-V-Mo dual-phase alloys. *Acta Mater.* **198**, 271-280 (2020).
16. Huang, R., *et al.* Giant negative thermal expansion in NaZn$_{13}$-type La(Fe, Si, Co)$_{13}$ compounds. *J. Am. Chem. Soc.* **135**, 11469-11472 (2013).